IEEE Robotics and Automation Letters (RAL) paper presented at
2024 IEEE/RSJ International Conference on Intelligent Robots and Systems (IROS)
October 14-18, 2024. Abu Dhabi, UAE

Mitigating Collision Forces and Improving Response Performance in Human-Robot Interaction by Using Dual-Motor Actuators

Amin Khorasani, *Graduate Student Member, IEEE*, Muhammad Usman, Thierry Hubert, Raphaël Furnémont, Dirk Lefeber, Bram Vanderborght, and Tom Verstraten, *Member, IEEE*

***Abstract*—In collaborative robotics, the safety of humans interacting with cobots is crucial. There is a need for collaborative robots that can move quickly while still being safe. This letter introduces the use of a kinematically redundant actuator in impedance control mode to reduce collision forces, aiming to improve both the safety and efficiency of collaborative robots. By distributing power across multiple drive-trains, each with unique properties such as reflected inertia, the actuator's behavior during collisions is optimized, which is key for safe interactions. Using theoretical analysis and practical experiments, we evaluate the response performance of the redundant actuator in various collision situations according to ISO/TS 15066, comparing it with that of a standard single-drive actuator. Our experiments show that the redundant actuator significantly lowers collision forces, with a 44% reduction in peak forces and an 81% decrease in transferred impulses during collisions. The letter concludes by offering a design parameter recommendation for designing actuators with reduced reflected inertia.**

***Index Terms*—Cobot, collision, dual motor actuator, pHRI, safety.**

I. INTRODUCTION

COBOTS are meant to perform all kinds of daily tasks as well as production processes in close or physical interaction with humans. During the interaction between humans and collaborative robots, it is important to ensure the safety of the user and those around the robot. The International Organization for Standardization (ISO) introduced ISO/TS 15066 in 2016 as a supplement to ISO 10218 standards, governing robotic safety, referenced in this letter as ISO/TS [1]. Collaborative robots must adhere to safety protocols outlined in ISO/TS, including safety-rated monitored stop, hand guiding, speed and separation monitoring, and power and force limiting. This letter emphasizes limiting power and force to minimize blunt collision impact, while existing literature also explores collision avoidance through speed and separation monitoring.

Several researchers have contributed to advancing safety measures for collaborative robots. For instance, Kirschner et al. [2] focused on enhancing human-robot safety by accurately determining the robot's moving mass, surpassing the basic model outlined in ISO/TS. They further explored various scenarios in different configurations, considering factors like the robot's proximity to singular workspaces and collision quality areas, as well as the possibility of human escape [3].

During robot-human collisions, injury results from contact geometry, collision speed, and perceived inertia [4]. Efforts to mitigate injury include incorporating soft structures into robot bodies, although altering payload surface quality may be challenging [5]. Compliance and impedance-based controllers have been extensively studied to enhance safety and predictability during human-robot interactions [6], [7], [8]. The robot's joints are also softened by introducing joint mechanisms to reduce impact during static collisions [9], [10], or with variable stiffness actuators (VSA) [11], [12], or series elastic actuators (SEA). SEAs, in particular, mitigate the impact of collisions by absorbing high forces, thereby shaping the collision behavior to be less harmful. While SEAs with low stiffness benefit from decoupling the reflected inertia from the actuator to the load, this advantage comes at the expense of decreased force control bandwidth and precision in positioning, which may not be suitable for all applications [13], [14].

Numerous studies have addressed speed control for safety, employing proximity sensing [15] and safety maps in workspace [16]. Researchers have also reduced robot inertia through methods such as link optimization [17], [18] and topology optimization [19]. Redundant kinematic structures have been utilized for tasks not requiring full robot degrees of freedom, optimizing robot configuration to minimize inertia during unexpected collisions [20].

Kinematically redundant actuators offer the potential to reduce energy consumption or provide a wider operating range than common actuators as discussed in detail in [21], and [22]. Additionally, we proposed a design methodology and selection of its components of the shelve to have a light and energy-efficient solution in [23]. In [24], researchers have demonstrated that the inertia of the actuator in certain working conditions

---

Manuscript received 18 December 2023; accepted 23 April 2024. Date of publication 2 May 2024; date of current version 16 May 2024. This letter was recommended for publication by Associate Editor Y. Hu and Editor G. Venture upon evaluation of the reviewers' comments. This work was supported by Research Foundation Flanders (FWO) SBO Project ELYSA Project under Grant S001821N. *(Corresponding Author: Amin Khorasani.)*

Amin Khorasani, Muhammad Usman, Thierry Hubert, Raphaël Furnémont, Dirk Lefeber, and Tom Verstraten are with Brubotics, Vrije Universiteit Brussel, 1050 Brussels, Belgium, and also with Flanders Make, 1050 Brussels, Belgium (e-mail: amin.khorasani@vub.be).

Bram Vanderborght is with Brubotics, Vrije Universiteit Brussel, 1050 Brussels, Belgium, and also with Imec, 1050 Brussels, Belgium.

This letter has supplementary downloadable material available at https://doi.org/10.1109/LRA.2024.3396370, provided by the authors.

Digital Object Identifier 10.1109/LRA.2024.3396370

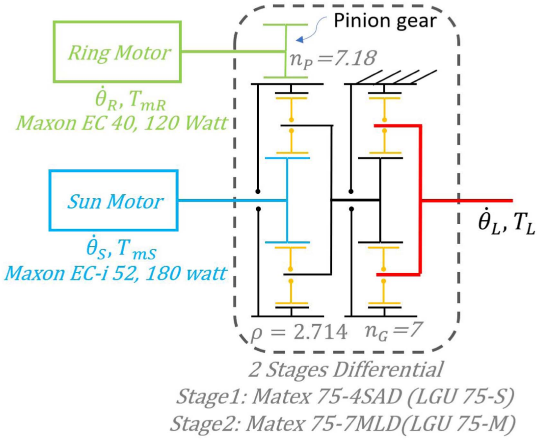

Fig. 1. DMA Schematics, consisting of 2 motors (Sun and Ring drive train) as the inputs and represented $\dot{\theta}_L$ as the output speed.

is lower than the inertia of both drive-trains individuals. This allows for minimizing perceived inertia during collisions with humans, enhancing cobot speed within ISO/TS safety thresholds. Reducing reflected inertia and using redundant actuators in impedance control mode can mitigate collision forces and improve response performance. This research demonstrates how redundancy enhances actuator safety.

In Section II, we outline the redundant actuator's design and mechanics, comparing its reflected inertia to that of a single-drive actuator (SDA). Section III examines human-robot collision dynamics, introduces an impedance control strategy for the redundant actuator, and assesses its performance through simulations, highlighting its advantages over SDA in collision scenarios. Section IV details the experimental collision tests and results for both actuators, while Section V provides design insights. Results and future research are discussed in the final section.

II. REDUNDANT ACTUATOR PRINCIPLES AND INERTIA IMPACT ON SELECTION

A. Structure, Kinematics, and Dynamics of DMA

Collaborative robot actuators typically consist of an electric motor paired with a high-ratio transmission. In contrast, the dual motor actuator (DMA), depicted in Fig. 1, is a kinematically redundant actuator that has been explored in [21] and [23] extensively.

This DMA comprises two motors, a differential, and an auxiliary gear set. As a kinematically redundant actuator, the DMA operates as a Multiple Input Single Output (MISO) control system with multiple input speeds producing a single output speed. The kinematics of this system is represented in the subsequent equation:

$$\dot{\theta}_L = R_S\dot{\theta}_S + R_R\dot{\theta}_R \tag{1}$$

$$R_S = \frac{1}{n_G(1+\rho)} \tag{2}$$

$$R_R = \frac{\rho}{n_G n_P(1+\rho)} \tag{3}$$

While $\dot{\theta}_L$ is the load (output) speed while $\dot{\theta}_S$ and $\dot{\theta}_R$ are the sun and ring drive-train motors (input) speed, respectively. ρ is the ring-to-sun gear ratio of the differential, n_G is the second stage gearbox ratio, and n_P is the ratio of the gear attached to the ring of the differential.

After the derivation of speed distribution, the acceleration distribution in a DMA can be expressed as follows:

$$\ddot{\theta}_L = R_S\ddot{\theta}_S + R_R\ddot{\theta}_R \tag{4}$$

A basic forward dynamic equation for the DMA is presented here.

$$\begin{bmatrix} T_{mS} \\ T_{mR} \end{bmatrix} = M \begin{bmatrix} \ddot{\theta}_S \\ \ddot{\theta}_R \end{bmatrix} + R_{SR}\left(T_v + T_c + T_L\right)$$

$$M = \begin{bmatrix} J_S + R_S^2(J_C + J_L) & (J_C + J_L)R_S R_R \\ (J_C + J_L)R_S R_R & J_R + R_R^2(J_C + J_L) \end{bmatrix}$$

$$R_{SR} = \begin{bmatrix} R_S \\ R_R \end{bmatrix} \tag{5}$$

T_{mS} is the torque on the sun drive-train motor, J_S is sun rotor inertia plus sun gear inertia, T_{mR} is the torque on the ring drive-train motor, J_R is ring rotor inertia plus pinion gear inertia, and J_C is carrier and second stage gearbox reflected inertia at output, and J_L accounts for load inertia effect. Also, T_v, T_c, and T_L are the viscous friction, Coulomb friction, and load torque, respectively, which are described as follows.

$$T_\nu = \begin{bmatrix} \nu_S\dot{\theta}_S \\ \nu_R\dot{\theta}_R \end{bmatrix}$$

$$T_c = \begin{bmatrix} \text{sign}\left(\dot{\theta}_R\right) T_{cS} \\ \text{sign}\left(\dot{\theta}_R\right) T_{cR} \end{bmatrix}$$

$$T_L = T_g + T_{\text{env}} \tag{6}$$

In this equation, ν_S, and ν_R are sun and ring drive-train viscous coefficients respectively. T_{cS}, ad T_{cR} are coulomb friction of both drive-trains. For calculating the load torque, $T_g = mgl\cos\theta_L$ is the gravitational effect of a simple link attached to the actuator. T_{env} is the environmental torque at the output joint during collisions, which is a function of the robot's geometric Jacobian and the reaction forces at the point or surface of collision.

The model here consolidates viscous T_ν and Coulomb friction T_c from bearings and gears without detailing individual component dynamics, unlike [21]. Additionally, it overlooks the inertia of the second gear stage in the differential due to its negligible impact on total reflected inertia. Stiction-friction and gear backlash are also disregarded. Gearbox backlash affects motor reaction performance and force estimation due to delay from backlash. This study uses the same gearboxes with equal backlash to compare SDA and DMA.

B. Reflected Inertia of DMA

As per ISO/TS guidelines, effective mass plays a crucial role in determining speed limits for varying payloads. However,

TABLE I
DMA DYNAMIC PARAMETERS

Sun (motor+gear) Inertia	$J_S = 185$ g.cm^2
Sun Drive-train Coulomb Friction	$T_{cS} = 12.3$ mNm
Sun Drive-train Viscous Friction	$\nu_S = 0.041$ mNm.s/rad
Ring (Motor+pinion) Inertia	$J_R = 95$ g.cm^2
Ring Drive train Coulomb Friction	T_{cR} = 3.8 mNm
Ring Drive train Viscous Friction	ν_R = 0.012 mNm.s/rad
Carrier+Second stage Inertia	$J_C = 0.8$ g.m^2
Output link Inertia	$J_L = 3.63$ g.m^2

The corresponding kinematic parameters are illustrated in the Fig. 1. Friction parameters are identified through experiments, while inertia terms are derived from the CAD model.

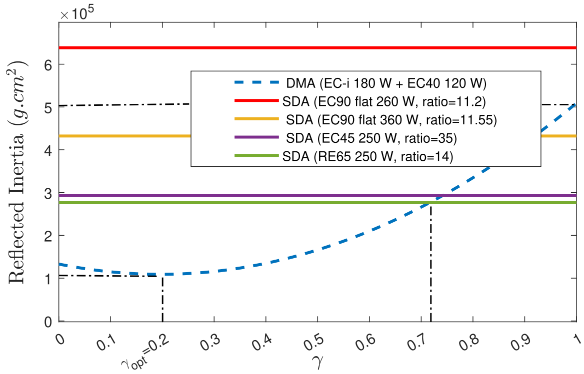

Fig. 2. Comparison of DMA reflected inertia (dashed line) with parameters similar to Fig. 1 at various speed distributions (γ) for the sun and ring drive-trains against multiple SDAs in the power range of 250 to 360 watts. For a fair comparison, the SDAs are selected with minimum gear ratios to match the torque capacity of 300-watts DMA. All SDAs can be equipped with an APEX-AB042 series with a constant inertia of 30 g.cm^2 for a wide range of ratios.

while ISO/TS defines effective mass based on payload and robot link masses, it overlooks the significant impact of actuator's reflected inertia. This inertia can be modulated through control, offering flexibility. In DMA systems with two drive trains, the total kinetic energy is a combination of both. Hence, optimizing the speed distribution minimizes the reflected inertia at the DMA output. In [24], the following equation was proposed to approximate the kinetic energy of the DMA in a lossless model by considering each drive-train contribution.

$$\frac{1}{2}J_{DMA,ref}(\gamma)\dot{\theta}_L^2 = \frac{1}{2}(J_C + J_L)\dot{\theta}_L^2 + \frac{1}{2}J_S\dot{\theta}_S^2 + \frac{1}{2}J_R\dot{\theta}_R^2 \tag{7}$$

The reflected inertia of the DMA, denoted as $J_{\mathrm{DMA,ref}}(\gamma)$, is a function of the speed distribution factor γ, defined as $\gamma = R_R\dot{\theta}_R/\dot{\theta}_L$. Optimal speed distribution for minimal reflected inertia of the actuator can be calculated using the methodology detailed in [24], and is expressed as follows:

$$\gamma_{opt} = \frac{R_R^2 J_S}{R_R^2 J_S + R_S^2 J_R} \tag{8}$$

In the given context, the reflected inertia of the DMA with parameters in Table I and Fig. 1 is compared with its single-drive actuator counterpart under various configurations. The corresponding SDAs are selected based on their torque compatibility, with an emphasis on minimizing the gear ratio. As shown in Fig. 2 the reflected inertia of this selected DMA is at a minimum when operating at the optimal speed ratio ($\gamma_{opt} = 0.2$). Furthermore, for $\gamma < 0.72$, the reflected inertia of the DMA is lower than that of an equivalent single-drive actuator. Importantly, this discussion on reflected inertia is based solely on the dynamic equations, not considering the controller's role in shaping the perceived inertia, which will be elaborated on in the subsequent section.

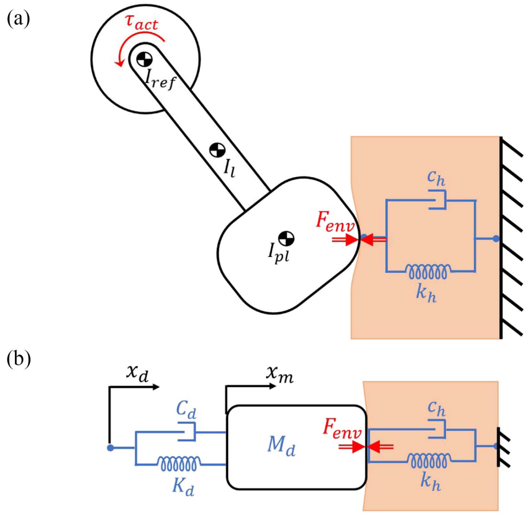

Fig. 3. (a) Collision of a rigid payload with a human body in a fully constrained situation while considering an actual robot without control effect. (b) Collision modeled as a compliant mass, spring, and damper system similar to the desired impedance model of the robot felt by the human body.

III. IMPEDANCE CONTROL OF DMA INTENDED FOR PHRI

This section provides an overview of the ISO norm and assumptions regarding human-robot configurations during collisions. It presents the impedance control block diagram for the redundant actuator, discussing error convergence during collisions and trajectory tracking in non-collision scenarios. Simulations evaluate the strategy's performance during collisions.

A. *Dynamic Behavior of Human-Robot Collisions*

This research aims to explore a redundant actuator's behavior in collision scenarios, considering blunt geometries and non-singular robot configurations aligned with ISO/TS guidelines. It assumes both the robot and its support structure remain rigid throughout. The interaction model in Fig. 3(a) illustrates a one-dimensional contact between the human and robot. Although the robot is represented as a single link for simplicity in Fig. 3(b), its behavior during the collision mirrors that of a mass, spring, and damper system in an impedance control setting. However, this representation may not perfectly align with the robot's physical characteristics.

According to ISO/TS, the robot's moving mass m_{R} is considered as half the mass of the robot's moving parts M and the whole mass of the payload m_{L}, if a human and payload collision occurs.

$$m_{\mathrm{R}} = \frac{M}{2} + m_{\mathrm{L}} \tag{9}$$

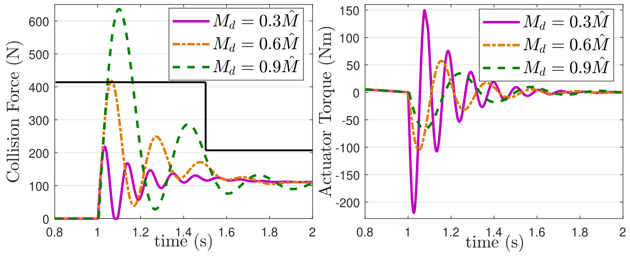

Fig. 4. Simulation of robot's blunt part impact on human abdomen. The left graph displays collision force response. The ISO norm allows a transient peak force of 420 N (solid black line) for 0.5 seconds, with steady-state force capped at 210 N. Reducing desired mass in the control loop reduces peak force during collision. Conversely, larger actuators are needed for increased torque.

While this basic formula is easy to use, it might not be accurate enough for specific situations. Recognizing this, researchers in [5] referred to Khatib's detailed model [25]. They suggested a more detailed way to determine the robot's effective mass at a point in a specific direction $m_u(\boldsymbol{q})$ considering the reflected inertia of the robot.

$$m_u(\boldsymbol{q}) = \left[\boldsymbol{u}^\top \boldsymbol{\Lambda}_v(\boldsymbol{q})^{-1}\boldsymbol{u}\right]^{-1} \tag{10}$$

In this equation, $\boldsymbol{u}$ is the collision direction, and $\boldsymbol{\Lambda}_v(\boldsymbol{q})$ is the translational mass matrix of the robot. The formulations primarily account for the robot's mechanical properties and its configuration, like what is depicted in the Fig. 3.a. In this case, the general dynamic model in interaction with the environment is:

$$\begin{aligned} M(\boldsymbol{q})\ddot{\boldsymbol{q}} + C(\boldsymbol{q},\dot{\boldsymbol{q}})\dot{\boldsymbol{q}} + \boldsymbol{g}(\boldsymbol{q}) &= \tau_{act} - \tau_{\text{env}} \\ \tau_{\text{env}} &= J^T(\boldsymbol{q})\boldsymbol{F}_{\text{env}} \end{aligned} \tag{11}$$

In this equation, $J^T(\boldsymbol{q})\boldsymbol{F}_{\text{env}}$ represents the interaction force impacting the actuator's torque, as previously described in Section II-A. However, as depicted in Fig. 3.b, the perceived impact during a collision may differ when considering the robot's compliant control strategies e.g. impedance control which defines robot behavior like a virtual mass, spring, and damper. In such instances, a robot with specific mechanical properties at a specific configuration behaves as a compliant system, where its mass behavior does not necessarily align with that presented in the ISO/TS or the more detailed model in (10). Fig. 4 illustrates an impact simulation that demonstrates how mechanical inertia felt by humans in a collision cannot be compared with what users experience if there is a small value for the desired virtual mass. The inertia experienced by humans can be equal to, higher than, or lower than the actual inertia of the robot and payload in this case. However, it should be noted that very low virtual mass cannot be defined in the control loop due to the limitations of actuators [26]. In this instance, actuator design is crucial in minimizing the severity of collisions and ensuring user safety. Lowering the virtual mass in a robot's control model increases its response to external forces, requiring actuators to generate more torque to stabilize the system, especially during impacts. This sensitivity explains why reducing virtual mass to minimize felt inertia has practical limits. To decrease collision inertia effectively, reducing the actuator's reflected inertia is essential, which is thoroughly discussed in section II. This balance is key to improving safety without overburdening the actuator's capabilities.

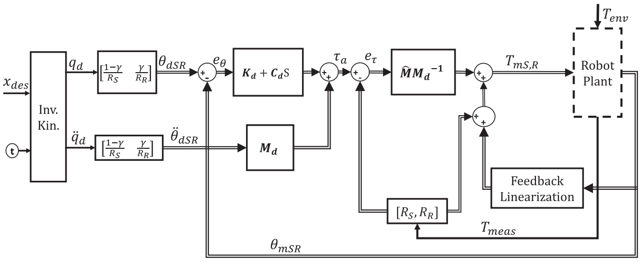

Fig. 5. Schematic of the impedance control strategy for a DMA.

B. Impedance Control of DMA

Current collaborative robots equipped with SDAs utilize impedance control to achieve desired impedance behaviors, ensuring physical safety. This approach translates the intricate robot behavior into a more comprehensible mass-spring-damper system, as showcased in Fig. 3.

In the meantime, DMA in impedance control mode as a MISO system requires attention to regulating the impedance behavior of two drive trains. The proposed impedance control scheme tailored for DMA is depicted in Fig. 5.

The closed-loop formulation for the proposed control by substitution of (5) and 6 into the robot plant model is determined by the following calculations:

$$\begin{aligned} &\mathbf{M}\ddot{\theta}_{SR} + \left(T_v + T_c + T_g + T_{\text{env}}\right) R_{SR} \\ &= \hat{\mathbf{M}}\mathbf{M_d}^{-1}\left\{\mathbf{M_d}\ddot{\theta}_{dSR} + \mathbf{C_d}\dot{e}_{\theta_{SR}} + \mathbf{K_d}e_{\theta_{SR}} - T_{\text{meas}}\, R_{SR}\right\} \\ &+ \left(\hat{T}_\nu + \hat{T}_c + \hat{T}_g + T_{\text{meas}}\right) R_{SR} \end{aligned} \tag{12}$$

$\boldsymbol{M}$ is the real inertia matrix of the system, $\hat{\boldsymbol{M}}$ is the estimated inertia matrix of the system. The terms $\hat{T}_\nu$, $\hat{T}_c$, and $\hat{T}_g$ are the estimated viscous, coulomb, and gravitational components of the dynamics, respectively, which are compensated for in the Feedback Linearization block. $\dot{e}_{\theta_{SR}}$ are tracking error speed of two motors, and $e_{\theta_{SR}}$ are tracking error on position of both motors. $\ddot{\theta}_{SR}$ are sun and ring motor acceleration matrix, and $\ddot{\theta}_{dSR}$ are desired sun and ring motor acceleration. T_{env} represents the environmental interaction torque at the joint, which ideally equals T_{meas} under perfect measurement conditions. The matrices $\boldsymbol{M_d}$, $\boldsymbol{C_d}$, and $\boldsymbol{K_d}$ are the desired mass, spring, and damper matrices, respectively. The following equivalencies are valid in an ideal estimation of robot dynamics, and measurements:

$$\hat{\boldsymbol{M}} \approx \boldsymbol{M}, \hat{T}_\nu \approx T_\nu, \hat{T}_c \approx T_c, \hat{T}_g \approx T_g, T_{\text{meas}} \approx T_{\text{env}} \tag{13}$$

Simplifying this closed-loop dynamic equation, considering mentioned equivalency between real and estimated terms, and performing basic calculations yields the following equation:

$$\mathbf{M_d}\ddot{e}_{\theta_{SR}} + \mathbf{C_d}\dot{e}_{\theta_{SR}} + \mathbf{K_d}e_{\theta_{SR}} = T_{meas}R_{SR} \tag{14}$$

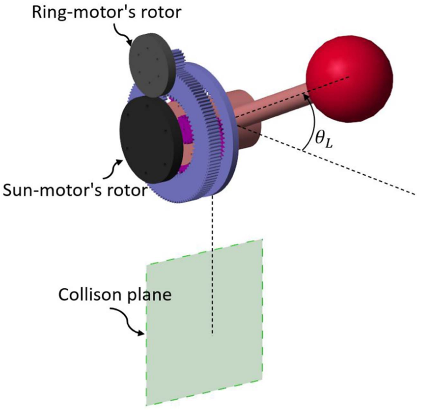

Fig. 6. 3D Simulation: DMA colliding with elastic plane.

By selecting each matrix accordingly and summing both rows of the equation, we obtain:

$$\mathbf{M_d} = \frac{1}{R_S + R_R}\begin{bmatrix} m_d R_S & 0 \\ 0 & m_d R_R \end{bmatrix}$$

$$\mathbf{C_d} = \frac{1}{R_S + R_R}\begin{bmatrix} c_d R_S & 0 \\ 0 & c_d R_R \end{bmatrix}$$

$$\mathbf{K_d} = \frac{1}{R_S + R_R}\begin{bmatrix} k_d R_S & 0 \\ 0 & k_d R_R \end{bmatrix} \tag{15}$$

$$m_d \underbrace{(R_S \ddot{e}_S + R_R \ddot{e}_R)}_{\ddot{e}_L}) + c_d \left(\underbrace{R_S \dot{e}_S + R_R \dot{e}_R}_{\dot{e}_L} \right)$$

$$+ k_d \left(\underbrace{R_S e_S + R_R e_R}_{e_L} \right) = T_{\text{meas}} \tag{16}$$

This implies that, under these conditions, the DMA's tracking performance in impedance control mode is equivalent to that of a single-drive actuator. Specifically, it behaves like a second-order dynamic system. Given positive values for the desired parameters, the system's response performance remains bounded.

C. Simulations and Discussion

To validate theoretical formulations and assess DMA performance, simulations were conducted using Simscape multi-body as depicted in Fig. 6. A virtual wall, mimicking the spring-like characteristics of the human body, was introduced to simulate realistic interactions. This allowed for an analysis of how each actuator, the DMA and the SDA, responds upon contact. The desired trajectories are depicted in Fig. 7. A virtual wall with 20 N/mm stiffness, mimicking the spring-like characteristics of the human body, is positioned to experience a normal collision with the link tip around t = 1 s. The impedance behavior has been adjusted to reflect the collision behavior depicted in Fig. 7, maintaining a trajectory tracking deviation of 0.01 rd before the collision event. The subsequent collision force can be observed in Fig. 7. For this scenario, the speed distribution is chosen optimally based on the (8). The results reveal that the peak force and transferred momentum using DMA, as depicted in Fig. 1, are notably lower than those observed with an equivalent best-inertia SDA, as represented in Fig. 2.

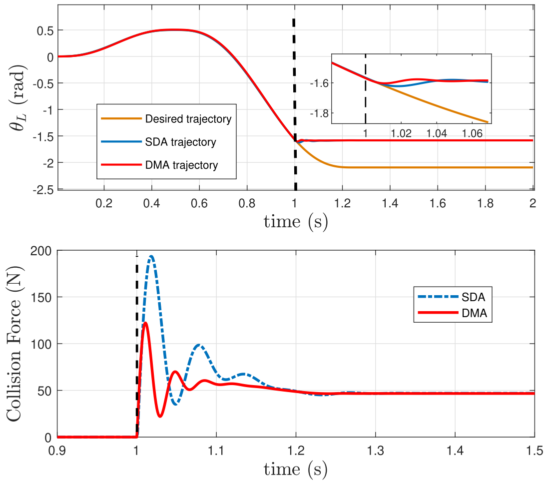

Fig. 7. (a) Tracking performance shows deeper SDA penetration during collision at $time = 1(s)$. (b) Collision force comparison illustrates DMA's reduced peak force and momentum for safer human-robot interactions.

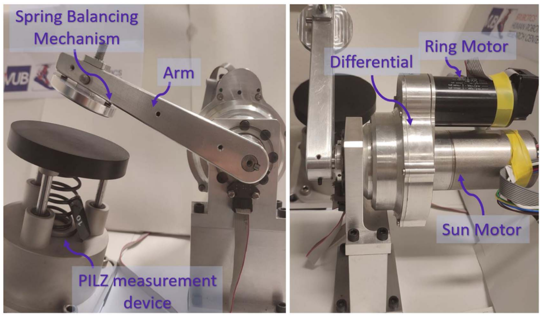

Fig. 8. Collision simulation setup. A DMA with potential to converting a SDA is utilized to study collison behaviour.

IV. EXPERIMENTAL SETUP

To validate the simulation results and examine the collision behavior in interactions similar to those with a human body, a test setup was designed around the proposed DMA (detail in Table I) and is depicted in Fig. 8. The lever arm connected to the actuator has been designed with a dual-balancing spring pivot component, to maintain a perpendicular force direction relative to its rotational axis and provide blunt collisions discussed in III-A.

In the following experiments, the Pilz Robot Measurement System (PRMS)[1] was employed to obtain precise collision measurements. This certified tool strictly adheres to the ISO/TS 15066 standards. The PRMS, with its capability to sample data at 2 kHz, promises accurate force readings. An important aspect of the PRMS is its set of springs and rubber covers, crafted to mirror the stiffness of various human body parts.

---

[1] https://www.pilz.com/en-INT/products/robotics/prms/prms

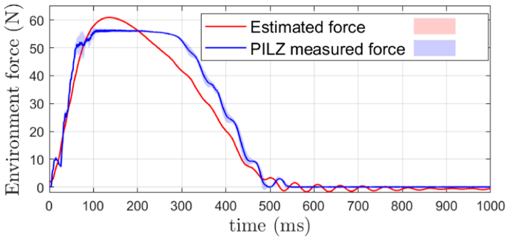

Fig. 9. Comparison of collision force measured by the PILZ setup with the force estimated from current measurements in an SDA collision test.

The right-hand side of (12) depicts the applied torque signal to each motor, equivalent to the measured torque value under ideal conditions. Subtracting the known dynamic model from the equation's left-hand side of this equation allows for estimating the environment's applied torque to the joint by averaging two identical recorded values. Therefore, the following equation can be used to estimate the environmental torque:

$$T_{meas} = \frac{1}{2}\sum_{i=S,R}\frac{1}{R_i}\left(\tau_{m,i} - \left(\hat{M}_i\ddot{\theta}_i + \hat{T}_{\nu,i} + \hat{T}_{c,i} + \hat{T}_g\right)\right) \tag{17}$$

Here, $\tau_{m,i}$ represents each motor's torque measurement.

The primary experiment of this study examines the behavior of collisions, their peak force, and transferred impulse during the collision under various scenarios. In the first experiment, the ring motor is mechanically locked, causing the differential to operate similarly to a traditional planetary gearbox. As a result, the system functions as an SDA rather than a DMA. Under this condition, unexpected collisions arise, assuming a collision occurs with a human hand, specifically when fingers are caught between the robot link and a rigid surface. The values for the desired impedance setting are chosen to ensure the tracking error of the desired trajectory remains within 0.05 rd and a collision happens at a speed of 0.7 m/s which is within the practical speed range for cobots when examining the ISO/TS. The collision was recorded using the Pilz setup for several tries, and the results of these collisions can be observed in Fig. 9. The recorded peak force for this event is 57 N, and upon integration over time, the resultant average impulse during the collision amounts to 19.8 Ns. A comparison between the estimated and measured forces during a collision reveals a deviation of 4 N in the peak force measurement. This discrepancy can be attributed to inaccuracies in the simulation model and unmodeled dynamic components, such as the compliance of the transmission. Additionally, it is evident that the estimated peak force declines more rapidly than the measured one. This can be due to multiple reasons. Firstly, the entire dynamic behavior of the system may not have been captured in the model. Secondly, the use of a low-pass filter to estimate the environmental force can potentially dampen and attenuate high-frequency components, causing the estimated force to decay faster than the actual measured force.

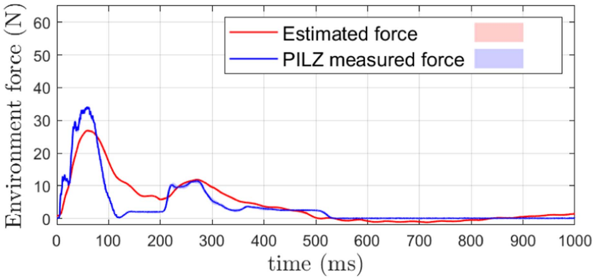

Fig. 10. Collision force response measured while DMA is active and $\gamma = 0$, leading to a peak force of 34 N.

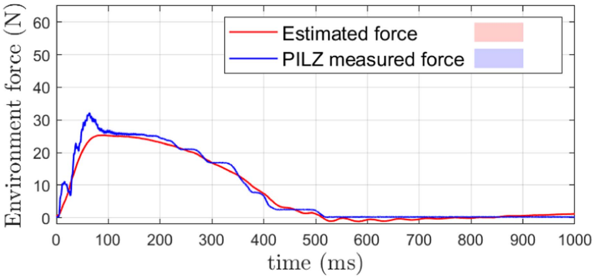

Fig. 11. Measured collision force while both motors on the DMA working with optimal speed ratio. In this case, the measured peak force is 32 N.

In the second experiment, the ring motor is unlocked, so there is DMA in action, and initial settings are adjusted for minimal desired stiffness and damping in this branch. This experiment ensures the ring drive train remains stationary when there is no collision and $\gamma = 0$ in the control loop. It also provides adequate stiffness and damping to account for any inaccuracies in the estimated environmental force when there is not any collision, seen to be around 4 N as shown in Fig. 9 after 600 ms time. In Fig. 10, the PILZ setup shows a pronounced decrease in peak collision forces to 34 N, a 39% reduction from earlier results. The collision impulse also drops to 3.7 N.s, marking an 81% decrease.

In the third experiment, the optimal speed distribution of DMA was examined with $\gamma = \gamma_{opt} = 0.2$. It was observed that with consistent tracking behavior, it is feasible to decrease the peak force of using a DMA in its optimal speed distribution, for having minimum reflected inertia, by 44% in comparison to SDA, and average impulse also reduced to 8.5 Ns. The results from this experiment are illustrated in Fig. 11. In this scenario, we observe a decrease in peak force but an increase in impulse compared to the second experiment. This is because the drive train with lower kinetic energy needs to stop and reverse to absorb energy from the other drive train, unlike in the previous scenario where the stationary ring drive train could quickly absorb kinetic energy upon collision.

V. Design Guidelines and Discussion

In prior sections, we analyzed the role of redundant actuators in mitigating peak collision forces. While they can effectively reduce these forces, one can wonder if they always outperform response performance of common SDAs. Key to this investigation is the reflected inertia of the actuator, crucial for reducing the collision force.

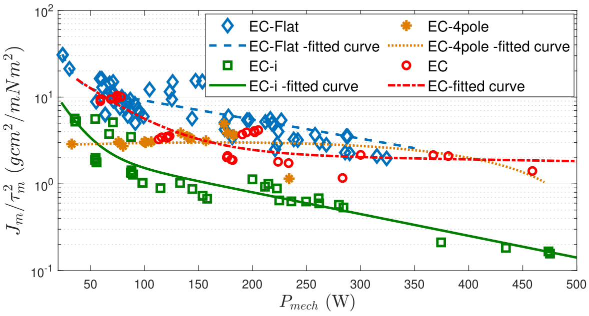

Fig. 12. Comparison of the parameter J_m/τ_m^2 as a candidate reflecting inertia behavior across different mechanical power levels for Maxon brush-less motor series.

To assess this question, let us consider an actuator capable of handling an output load, denoted as τ_L as maximum load, while operating at a speed represented by $\dot{\theta}_L$. Given that many collaborative robotic applications have actuators limited to 30-40 RPM, speed becomes less critical. This desired output can be achieved using a high-torque motor (τ_m) with minimal gear reduction (n) or its low-torque counterpart with significant gear reduction. With planetary gearboxes like the Apex AP series, which maintain high efficiency (above 92%) even at extensive gear ratios (up to 400), we can reasonably consider a constant gearbox efficiency η for our analysis.

$$\begin{aligned}&\tau_L = \eta\tau_m n\\ &J_{ref} = J_m n^2 \Longrightarrow J_{ref} = J_m\left(\frac{\tau_L}{\tau_m\eta}\right)^2 \Longrightarrow J_{ref} \propto \frac{J_m}{\tau_m^2}\end{aligned} \tag{18}$$

In this equation, load torque (τ_L) is affected by factors including gearbox ratio (n), efficiency (η), and motor nominal torque (τ_m). Meanwhile, rotor reflected inertia (J_{ref}) depends on rotor inertia (J_m) and the square of the gear ratio. Substituting the gear ratio into the equation reveals a direct proportionality between motor inertia and reflected inertia, inversely proportional to torque squared. Other scaling laws explored in studies like [27] investigate the relationship between Maxon motor inertia and torque.

Fig. 12 illustrates this relationship across various Maxon motor series. Actuators with powerful motors tend to exhibit lower reflected inertia compared to those with low-power motors and high gear ratios for a specific torque requirement. This highlights the advantages of high-torque, low-gear-reduction configurations, especially in applications where reflected inertia significantly impacts performance, such as in cobots and haptic devices. Among the examined EC Maxon motor series, the ECI-i Series shows minimal parameter values, particularly in mid to high-power scenarios, while high-torque EC-Flat motors demonstrate the highest values. However, it's noteworthy that the ECI-i Series motors are heavier compared to other series like the EC-Flat. Selecting motors from the Maxon categories showcased in Fig. 12 allows for the creation of numerous DMA combinations. To ensure a valid comparison with SDA, the overall power of both actuator types is aligned. Additionally, with a set output torque requirement (e.g., 1 N.m in this study), the minimum gear ratios are adjusted according to each motor's torque capacity, whether for the DMA's sun or ring drive-train, or the SDA's motor.

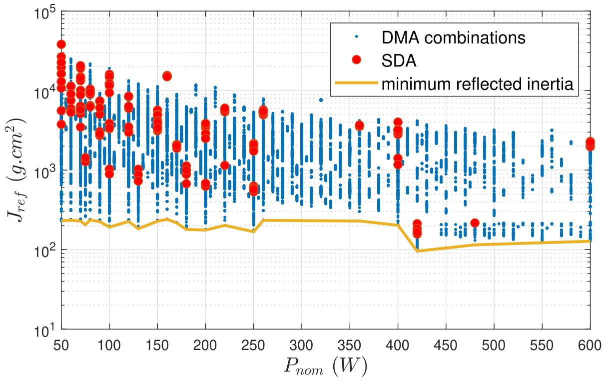

Fig. 13. Comparison of DMA's minimum reflected inertia with equivalent SDA configurations from Maxon's EC-i, EC, EC-Flat, and EC-4pole series. The orange line indicates the minimum reflected inertia for DMAs at power levels where an SDA is available.

With the components for both DMA and SDA selected, the optimal speed distribution for minimizing DMA's inertia is determined using (8). Applying this value in the (7) calculates the optimal reflected inertia for the DMA. In this analysis, the carrier and load inertia are considered consistent across all configurations.

The results of this approach are depicted in Fig. 13, where blue dots indicate the reflected inertia for different DMA configurations across various nominal powers. Similarly, the red dots represent the reflected inertia for SDA configurations using a range of Maxon motors. These findings underscore the importance of selecting DMA configurations from the designated Maxon motor range, which consistently results in lower reflected inertia. This reduction enhances safety in human-robot interactions. The minimum reflected inertia for DMA configurations under 250 W ranges from 230 to 170 g.cm^2, in contrast to the corresponding SDA minimum reflected inertia which varies between 3700 to 540 g.cm^2. This reflects an increase of 317% for the SDA over the DMA, even in the most favorable scenario. Furthermore, while the power range from 250 to 400 W presents numerous DMA combinations, there are only a few SDA options. At a power level of 420 W, the SDA's reflected inertia reaches its minimum at 157 g.cm^2, yet its DMA counterpart is calculated at only 96 g.cm^2, marking a 39% decrease relative to the SDA.

VI. CONCLUSION AND FUTURE WORK

A DMA offers distinct advantages in cobot applications by mitigating collision forces compared to traditional SDAs, particularly in scenarios involving direct human-robot interactions or unexpected collisions. Our DMA prototype showcased a notable 44% reduction in peak collision force and an 81% decrease in collision impulse compared to single-motor setups. We also provide design guidelines focusing on minimizing the actuator's reflected inertia, introducing a normalized parameter for comparison across various Maxon motors. High-power actuators exhibit lower reflected inertia compared to low-power, high gear ratio configurations.

Moreover, the optimal reflected inertia of a DMA often proves to be lower than that of a SDA, which can significantly reduce the potential for injuries in human-robot interactions. Furthermore, utilizing a DMA, with its reduced reflected inertia, can enhance the cobot's operational speed while maintaining safety.

However, it is noteworthy that when one drive-train is mostly committed to safety, it consumes more energy, increases actuator mass, and requires an additional driver and complicated controller strategy. This leads to an essential inquiry: What is the net safety gain over these additional costs for a particular task when utilizing a DMA? Exploring this aspect could profoundly influence future research on the design of safe cobot actuators leveraging DMA.

One potential approach could involve using a drive train solely as a safety measure, activating it only during collisions. Under this approach, the stationary drive train could be designed with its thermal constraints in mind to prevent winding overheating during high torque and rotor acceleration in collisions. Such a method might allow for a more compact and lighter actuator design while maintaining safe human-robot interactions.

Improving multi-DOF kinematic arms during collisions remains an open challenge. Identifying which joints benefit most from DMAs and understanding the impact of safer, yet heavier, DMAs on arm dynamics are critical questions for future exploration. Beyond DMAs, comparing other technologies that mitigate collision forces and enhance robot performance is vital. Future work will focus on metrics such as adaptability to multi-DOF configurations, cost, maintenance, reliability, safety in faults, and performance across various speeds and payloads, paving the way for a comprehensive comparison of safe actuators for the next generation of collaborative robots.

REFERENCES

[1] O. I. de Normalización, “ISO-TS 15066: Robots and robotic devices: Collaborative robots,” ISO, 2016.

[2] R. J. Kirschner, N. Mansfeld, S. Abdolshah, and S. Haddadin, “Experimental analysis of impact forces in constrained collisions according to ISO/TS 15066,” in *Proc. IEEE Int. Conf. Intell. Saf. Robot.*, 2021, pp. 1–5.

[3] R.-J. Kirschner, N. Mansfeld, S. Abdolshah, and S. Haddadin, “ISO/TS 15066: How different interpretations affect risk assessment,” 2022, *arXiv:2203.02706*.

[4] T. Steinecker et al., “Mean reflected mass: A physically interpretable metric for safety assessment and posture optimization in human-robot interaction,” in *Proc. Int. Conf. Robot. Automat.*, 2022, pp. 11209–11215.

[5] M. Hamad, N. Mansfeld, S. Abdolshah, and S. Haddadin, “The role of robot payload in the safety map framework,” in *Proc. IEEE/RSJ Int. Conf. Intell. Robots Syst.*, 2019, pp. 195–200.

[6] S. B. Liu and M. Althoff, “Online verification of impact-force-limiting control for physical human-robot interaction,” in *Proc. IEEE/RSJ Int. Conf. Intell. Robots Syst.*, 2021, pp. 777–783.

[7] S. Jlassi, S. Tliba, and Y. Chitour, “An online trajectory generator-based impedance control for co-manipulation tasks,” in *Proc. IEEE Haptics Symp.*, 2014, pp. 391–396.

[8] M. Sharifi, V. Azimi, V. K. Mushahwar, and M. Tavakoli, “Impedance learning-based adaptive control for human–robot interaction,” *IEEE Trans. Control Syst. Technol.*, vol. 30, no. 4, pp. 1345–1358, Jul. 2022.

[9] Z. Niu et al., “Towards safe physical human-robot interaction by exploring the rapid stiffness switching feature of discrete variable stiffness actuation,” *IEEE Robot. Automat. Lett.*, vol. 7, no. 3, pp. 8084–8091, Jul. 2022.

[10] J.-J. Park and J.-B. Song, “Safe joint mechanism using inclined link with springs for collision safety and positioning accuracy of a robot arm,” in *Proc. IEEE Int. Conf. Robot. Automat.*, 2010, pp. 813–818.

[11] B. Vanderborght et al., “Variable impedance actuators: A review,” *Robot. Auton. Syst.*, vol. 61, no. 12, pp. 1601–1614, 2013.

[12] R. Mengacci, M. Garabini, G. Grioli, M. G. Catalano, and A. Bicchi, “Overcoming the torque/stiffness range tradeoff in antagonistic variable stiffness actuators,” *IEEE/ASME Trans. Mechatron.*, vol. 26, no. 6, pp. 3186–3197, Dec. 2021.

[13] H. Toubar, M. I. Awad, M. N. Boushaki, Z. Niu, K. Khalaf, and I. Hussain, “Design, modeling, and control of a series elastic actuator with discretely adjustable stiffness (seadas),” *Mechatronics*, vol. 86, 2022, Art. no. 102863.

[14] A. L. Junior, R. M. de Andrade, and A. Bento Filho, “Series elastic actuator: Design, analysis and comparison,” *Recent Adv. Robot. Syst.*, vol. 1, no. 3, 2016.

[15] P. Chemweno and R.-J. Torn, “Innovative safety zoning for collaborative robots utilizing kinect and LiDAR sensory approaches,” *Procedia CIRP*, vol. 106, pp. 209–214, 2022.

[16] N. Mansfeld, M. Hamad, M. Becker, A. G. Marin, and S. Haddadin, “Safety map: A unified representation for biomechanics impact data and robot instantaneous dynamic properties,” *IEEE Robot. Automat. Lett.*, vol. 3, no. 3, pp. 1880–1887, Jul. 2018.

[17] A. Albu-Schäffer, S. Haddadin, C. Ott, A. Stemmer, T. Wimböck, and G. Hirzinger, “The DLR lightweight robot: Design and control concepts for robots in human environments,” *Ind. Robot: Int. J.*, vol. 34, no. 5, pp. 376–385, 2007.

[18] M. Hu, H. Wang, and X. Pan, “Multi-objective global optimum design of collaborative robots,” *Struct. Multidisciplinary Optim.*, vol. 62, pp. 1547–1561, 2020.

[19] G.L. Srinivas and A. Javed, “Topology optimization of rigid-links for industrial manipulator considering dynamic loading conditions,” *Mechanism Mach. Theory*, vol. 153, 2020, Art. no. 103979.

[20] N. Mansfeld, B. Djellab, J. R. Veuthey, F. Beck, C. Ott, and S. Haddadin, “Improving the performance of biomechanically safe velocity control for redundant robots through reflected mass minimization,” in *Proc. IEEE/RSJ Int. Conf. Intell. Robots Syst.*, 2017, pp. 5390–5397.

[21] T. Verstraten et al., “Modeling and design of an energy-efficient dual-motor actuation unit with a planetary differential and holding brakes,” *Mechatronics*, vol. 49, pp. 134–148, 2018.

[22] T. Verstraten, C. Schumacher, R. Furnémont, A. Seyfarth, and P. Beckerle, “Redundancy in biology and robotics: Potential of kinematic redundancy and its interplay with elasticity,” *J. Bionic Eng.*, vol. 17, pp. 695–707, 2020.

[23] A. Khorasani et al., “A methodology for designing a lightweight and energy-efficient kinematically redundant actuator,” *IEEE Robot. Automat. Lett.*, vol. 7, no. 4, pp. 10786–10793, Oct. 2022.

[24] T. Verstraten, R. Furnémont, P. Lopez-Garcia, D. Rodriguez-Cianca, B. Vanderborght, and D. Lefeber, “Kinematically redundant actuators, a solution for conflicting torque–speed requirements,” *Int. J. Robot. Res.*, vol. 38, no. 5, pp. 612–629, 2019.

[25] O. Khatib, “Inertial properties in robotic manipulation: An object-level framework,” *Int. J. Robot. Res.*, vol. 14, no. 1, pp. 19–36, 1995.

[26] S. P. Buerger, “Stable, high-force, low-impedance robotic actuators for human-interactive machines,” Ph.D. dissertation, Massachusetts Inst. Technol., Cambridge, MA, USA, 2005.

[27] E. Saerens et al., “Scaling laws for robotic transmissions,” *Mechanism Mach. Theory*, vol. 140, pp. 601–621, 2019.